Gyrokinetic modeling of impurity peaking in JET H-mode plasmas

P. Manas, Y. Camenen, S. Benkadda, H. Weisen, C. Angioni, F. J. Casson, C. Giroud, M. Gelfusa, M. Maslov, and

Citation: Physics of Plasmas **24**, 062511 (2017);

View online: https://doi.org/10.1063/1.4985330

View Table of Contents: http://aip.scitation.org/toc/php/24/6

Published by the American Institute of Physics

Gyrokinetic modeling of impurity peaking in JET H-mode plasmas

P. Manas,[1,2] Y. Camenen,[2] S. Benkadda,[2] H. Weisen,[3] C. Angioni,[1] F. J. Casson,[4] C. Giroud,[4] M. Gelfusa,[5] M. Maslov,[4] and JET contributors[a)]
[1]*Max-Planck-Institut für Plasmaphysik, D-85748 Garching, Germany*
[2]*Aix-Marseille Université, CNRS, PIIM UMR7345, 13397 Marseille, France*
[3]*Ecole Polytechnique Fédérale de Lausanne (EPFL), Swiss Plasma Center (SPC), CH-1015 Lausanne, Switzerland*
[4]*CCFE, Culham Science Centre, Abingdon OX14 3DB, United Kingdom*
[5]*Department of Industrial Engineering, University of Rome "Tor Vergata," via del Politecnici 1, Roma, Italy*

(Received 13 February 2017; accepted 4 May 2017; published online 20 June 2017)

Quantitative comparisons are presented between gyrokinetic simulations and experimental values of the carbon impurity peaking factor in a database of JET H-modes during the carbon wall era. These plasmas feature strong NBI heating and hence high values of toroidal rotation and corresponding gradient. Furthermore, the carbon profiles present particularly interesting shapes for fusion devices, i.e., hollow in the core and peaked near the edge. Dependencies of the experimental carbon peaking factor (R/L_{n_C}) on plasma parameters are investigated via multilinear regressions. A marked correlation between R/L_{n_C} and the normalised toroidal rotation gradient is observed in the core, which suggests an important role of the rotation in establishing hollow carbon profiles. The carbon peaking factor is then computed with the gyrokinetic code GKW, using a quasi-linear approach, supported by a few non-linear simulations. The comparison of the quasi-linear predictions to the experimental values at mid-radius reveals two main regimes. At low normalised collisionality, ν_*, and $T_e/T_i < 1$, the gyrokinetic simulations quantitatively recover experimental carbon density profiles, provided that rotodiffusion is taken into account. In contrast, at higher ν_* and $T_e/T_i > 1$, the very hollow experimental carbon density profiles are never predicted by the simulations and the carbon density peaking is systematically over estimated. This points to a possible missing ingredient in this regime. [http://dx.doi.org/10.1063/1.4985330]

I. INTRODUCTION

Understanding impurity transport in the core of tokamak plasmas is central to achieving controlled fusion. Indeed, impurities are ubiquitous in these devices, and their presence in the core is detrimental to plasma confinement (fuel dilution and Bremsstrahlung). Thus, impurity transport modeling is a crucial topic widely addressed in the literature (e.g., Ref. 1 and references therein). Combined neoclassical and gyrokinetic simulations have come to a point where quantitative comparisons with experimental observations can be performed for light[2–11] and heavy impurities.[12,13]

In this context, a database of NBI heated H-mode JET plasmas (during the carbon wall era), which has been used for particle and momentum transport studies,[14–16] has also been extended to include intrinsic carbon impurity density profiles and is scrutinised with an emphasis on carbon transport. This database is particularly interesting for quantitative comparisons with numerical simulations as it mainly consists of flat/hollow core impurity profiles (attractive with respect to impurity accumulation) and strong normalised toroidal rotation and ion temperature gradients, which suggests strong convections via thermo-diffusion[17] and rotodiffusion.[18] The latter is a relatively new mechanism and has been found experimentally relevant for light impurity modeling in Refs. 2 and 3. Thus, it could play a nonnegligible role in the NBI heated JET discharges of this study.

The modeling of the neoclassical and turbulent transport is performed with the neoclassical code NEO[19] and the gyrokinetic code GKW,[20] respectively. In this study, a statistical approach is adopted, i.e., considering a large number of discharges and spanning a wide plasma parameter space. To achieve a large number of simulations at a reasonable computational cost, a quasi-linear approach is adopted. For a few cases, non-linear simulations are performed to verify the quasi-linear model. The objectives of this study are twofold: characterising the main experimental correlations between the carbon peaking factor and the plasma parameters and performing quantitative comparisons between theoretical and experimental carbon peaking factors to assess the impact of rotodiffusion in the development of these carbon hollow profiles.

This paper is organised as follows: In Sec. II, the database of JET H-modes is described. Multilinear regressions are performed, and the dependencies of the carbon peaking factor on the plasma parameters are underlined. In Sec. III, the method applied to compute R/L_{n_C} from neoclassical and gyrokinetic simulations is described in detail. Finally, in Sec. IV, results from these simulations are compared to experimental values of R/L_{n_C}, and conclusions are drawn.

[a)]See the Appendix of F. Romanelli *et al.*, Proceedings of the 25th IAEA Fusion Energy Conference 2014, Saint Petersburg, Russia. See the author list of "Overview of the JET results in support to ITER" by X. Litaudon *et al.* to be published in Nuclear Fusion Special issue: overview and summary reports from the 26th Fusion Energy Conference (Kyoto, Japan, 17–22 October 2016).

II. EXPERIMENTAL JET DATABASE

A. Plasma parameters and profiles

The database used in this study consists of 156 stationary state phases of deuterium plasmas with improved magnetic equilibrium reconstruction (computed using experimental measurements to constrain the current density profile in EFIT[21]). These plasmas are dominantly heated by Neutral Beam Injection (8 to 22 MW) and in some cases by Ion Cyclotron Resonance Heating (0 to 6 MW). The database was used in previous studies to characterise non-diffusive momentum transport and particle peaking dependencies[14–16] and has been extended to include carbon profiles. In the present study, emphasis is then given to the carbon transport. A wide range of plasma parameters is covered: plasma current, $I_p = 1$–2.6 MA; safety factor at 95% of the poloidal magnetic flux, $q_{95} = 2.4$–6; central electron density, $n_e = 2.6$–7.6×10^{19} m^{-3}; toroidal magnetic field strength, $B_T = 1.35$–3.4 T; and central deuterium Mach number, $M_D = 0.14$–0.38 (defined as $M_D = R\Omega/v_{th,i}$ with $v_{th,i} = \sqrt{2T_i/m_i}$ the ion thermal velocity and Ω the toroidal angular rotation frequency). The electron density and temperature are measured via Thomson scattering. The carbon density, temperature, and toroidal rotation are measured via Charge Exchange Recombination Spectroscopy[22] on the C^{5+} $N = 8$ to 7 line at 529.1 nm.

In Fig. 1, typical profiles of the carbon density, ion temperature, and toroidal angular rotation frequency (carbon toroidal velocity divided by the major radius at the low field side midplane) are shown together with their corresponding normalised gradients $R/L_x = -(R/x)(\partial x/\partial r)$, with R the major radius, r the minor radius, and x the considered quantity. The normalised gradients and their respective error bars (essential for meaningful comparisons with gradient driven simulation results) are computed following the same methodology as in Appendix A of Ref. 23. The carbon profile is hollow in the core and peaked close to the edge of the plasma. These profiles are typical of the database, and their nature (no impurity accumulation in the core) gives strong incentive for quantitative modeling. Due to the high level of NBI in these discharges, the normalised toroidal rotation gradient, $u' = (R^2/v_{th,i})\partial\Omega/\partial r$, and ion temperature gradient, R/L_{T_i}, are rather high, which motivates to investigate the role of the associated impurity convection mechanisms in the sustainment of hollow impurity profiles.

We note that intermittent transport processes can affect the plasma profiles from $r/a = 0$ to $r/a = 0.4$ for sawteeth and from $r/a = 0.8$ to $r/a = 1$ for edge localised modes (ELMs). The modeling, which does not include these transient mechanisms, is, therefore, restricted to r/a = 0.55. It has been checked for several particular cases, including hollow carbon profiles, that the sawteeth do not lead to a significant modulation of the carbon density profile. For two particular cases in Sec. IV, the analysis is extended to a wider radial range, $0.45 < r/a < 0.85$.

B. Multilinear regressions of the carbon peaking factor

Before addressing numerical simulations and comparisons with the experiment, multilinear regressions are performed on the database to identify the plasma parameters on which the carbon peaking factor R/L_{n_C} depends.

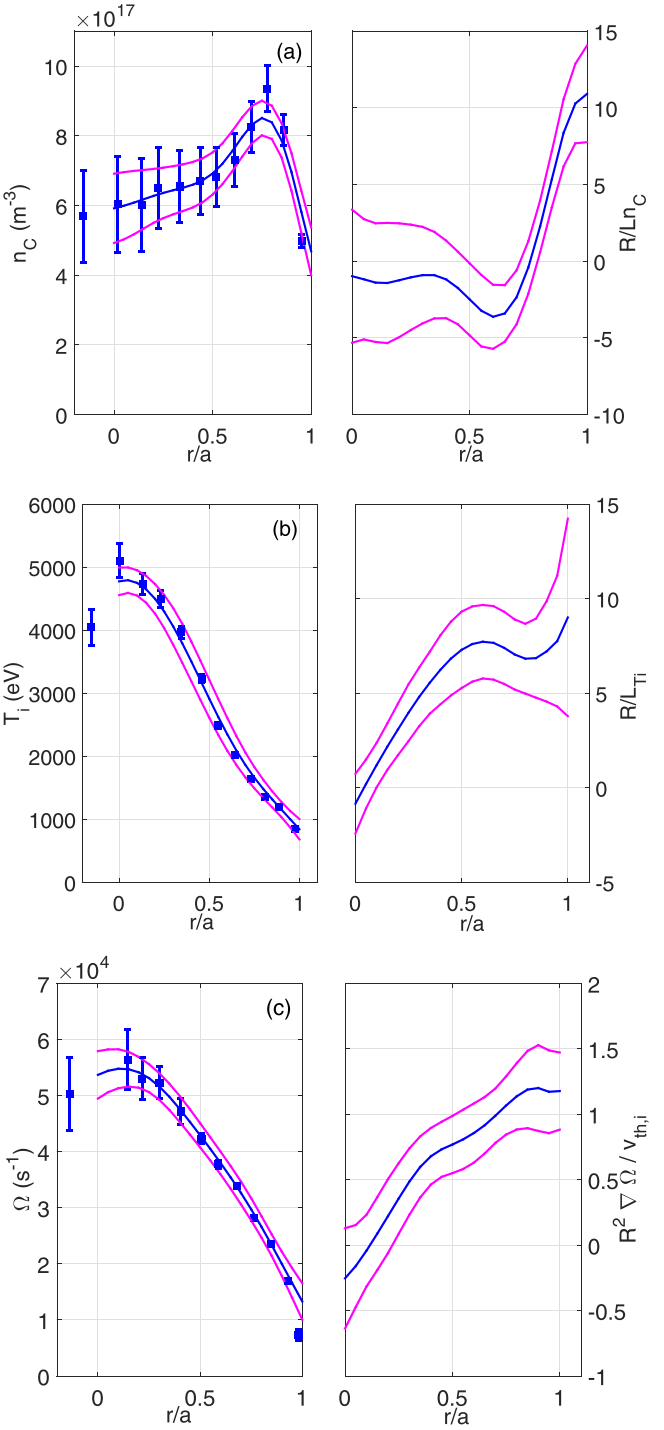

FIG. 1. Mean profiles (blue lines) of carbon density (a), temperature (b), and angular velocity (c) together with their corresponding normalised gradients (right panels). Standard deviations (magenta lines) and experimental measurements (blue squares) are also represented.

Correlations are unavoidable and need to be kept in mind when considering multilinear regressions. The degree of correlation between the experimental parameters is assessed in Appendix A where a correlation coefficient is computed for the following set of variables: u', the logarithmic electron density gradient R/L_n, R/L_{T_i}, R/L_{T_e}, the ratio of the total plasma pressure to magnetic pressure $\beta = 2\mu_0 nT/B^2$, $\rho_* = \rho_i/a$ with

$\rho_i = m_i v_{th,i}/(eB)$ the ion Larmor radius, a the plasma minor radius at the last closed flux surface, the local safety factor q, the magnetic shear $\hat{s}$, the normalised collisionality $\nu_* = \nu_{ei} q/\epsilon^{3/2}$ with ν_{ei} the electron-ion collision frequency, T_e/T_i, M_D, and R/L_{n_C}. The parameters ν_*, ρ_*, and β are all evaluated at $r/a = 0.55$.

Several plasma parameters appear to be strongly correlated, with a correlation coefficient $r_c > 0.2$ in the table. We note three important correlations: the correlation between ν_* and R/L_n, which has been largely documented in the literature (e.g., Refs. 14 and 25) and is a result of the collisionality dependence of particle transport; the correlation between ν_* and T_e/T_i, and finally the correlation between R/L_{T_i} and u' which is expected in NBI heated plasmas. From the correlation table, it already appears that one cannot directly disentangle the impurity peaking associated with a convection driven by R/L_{T_i} or u' from regressions only.

Another point of interest is of course the correlations between R/L_{n_C} and the other parameters. Although r_c values are relatively small (<0.2), i.e., R/L_{n_C} values are scattered with respect to the linear fits, the dominant linear correlations are with R/L_n, $\hat{s}$, ν_*, T_e/T_i, and u'.

Keeping in mind these couplings, multilinear regressions of R/L_{n_C} are performed against any combination of five variables among the ensemble described above and used in Appendix A. The regressed $R/L_{n_C}^{reg}$ is of the following form:

$$\left(\frac{R}{L_{n_C}}\right)^{reg} = \sum_{i=1}^{5} b_i x_i + constant \tag{1}$$

with x_i the ith variable and b_i its associated linear coefficient. For each coefficient, the uncertainty δb and statistical significance $b/\delta b$ (see Ref. 24 for more details) are computed. The multilinear regressions are sorted as a function of the quality of the fit (standard deviation σ).

In Fig. 2, the best fit ($\sigma = 1.19$) is shown for $r/a = 0.55$ (blue squares). The linear trend due to extremal values of R/L_{n_C} is not recovered, and only a trend from $-4 < R/L_{n_C} < 1$ is found. To account for these extremal values, their weight has been artificially increased. While the general trend is now captured by this regression, the quality of this fit is reduced ($\sigma = 1.43$). The variables used for the regressions, their linear coefficients b, uncertainty δb, and statistical significance are shown in Table I. The most important parameters with respect to their statistical significance are u', R/L_n, and M_D. The negative coefficient corresponding to u' suggests an outward convection associated with this parameter, but as noted before, R/L_{T_i} and u' are strongly coupled in these discharges. Furthermore, the regression with artificial additional weights yield the same qualitative results with an increased coefficient for u', which could indicate a strengthened role of outward convection.

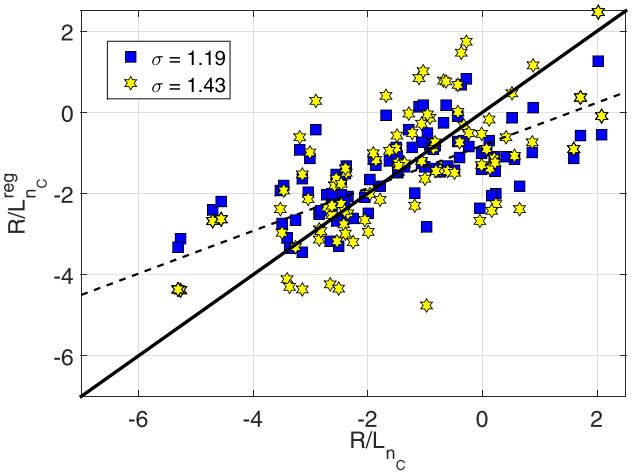

FIG. 2. Regressed versus experimental carbon peaking factor at $r/a = 0.55$. Regressions with (yellow hexagrams)/without (blue squares) artificially increased weights for $R/L_{n_C} < -4$ and $R/L_{n_C} > 1$ have been performed. The identity relation is shown with a full line, and the linear trend of the regression (blue squares) is highlighted by a dashed line. Parameters used in these regressions are gathered in Table I.

Due to the correlations between plasma parameters, one can obtain several regressions which present similar σ but with different variables. To take into account the fact that several fits of equivalent quality exist, the 10 best results are gathered in Table II. The number of occurrences of each variables is indicated, together with their mean statistical significance (computed from the 10 regressions), and the regressions are extended to the radial domain $r/a = 0.35$–0.85.

With respect to the occurrences, the best parameters to fit R/L_{n_C} at $r/a = 0.55$ are u', R/L_n, and M_D. The higher number of occurrences of u' compared to R/L_{T_i} could come from their correlation and cannot be interpreted as a weaker importance of R/L_{T_i}. For outer radii, R/L_{T_e} and $\hat{s}$ become dominant parameters with u' and R/L_n. This suggests an increasing role of electron turbulence such as trapped electron modes (dependent on $\hat{s}$) or electron temperature gradient modes (dependent on R/L_{T_e}) in the impurity transport channel but is not addressed in this study. Finally, u' and R/L_n are observed to be important parameters for the whole radial domain.

From these 10 best fits, one can then derive a mean linear coefficient for the variables u' and R/L_n at each radial position. This leads to Fig. 3 where the mean coefficients $\langle b \rangle$ together with their standard deviation are shown versus the normalised minor radius.

In the core, the negative values of $\langle b \rangle$ for u' again suggest an outward convection proportional to u' which flattens the profiles ($R/L_{n_C} \leq 0$). On the contrary, at the edge, $\langle b \rangle$ is positive, which now suggests an inward convection (peaked profiles, i.e., positive R/L_{n_C}). These observations seem to be

TABLE I. Variables used in multilinear regression of Fig. 2 together with their corresponding linear coefficients b, uncertainty δb, and statistical significance STS. The subscripts 1 and 2 correspond to the regression without and with additional weight on extremal values of R/L_{n_C}, respectively.

	b_1	b_2	δb_1	δb_2	STS_1	STS_2
u'	−1.94	−2.95	0.64	0.708	3.1	4.2
R/L_n	0.702	0.89	0.233	0.22	3	4.1
M_D	11.6	18.7	5.9	6.1	2	3.1
$\hat{s}$	−1.04	−2.06	0.914	0.88	1.1	2.4
R/L_{T_e}	−0.05	−0.16	0.24	0.23	0.22	0.67
Constant	−2.06	−1.47	2.16	2.25	0.95	0.65

TABLE II. Occurrences of the variables used in the 10 best multilinear regressions for several radial locations. The mean statistical significance (STS) is also shown. Occurrences above 6 and STS above 1 are highlighted in bold.

		u'	R/L_n	R/L_{T_i}	R/L_{T_e}	β	ρ_*	$\hat{s}$	q	ν_*	T_e/T_i	M_D
$r/a = 0.35$	Occurrences	**8**	**10**	3	5	2	1	2	**10**	2	1	6
	STS	**1.45**	**2.48**	1	0.05	0.3	0.16	0.34	**1.74**	0.32	0.03	1.35
$r/a = 0.45$	Occurrences	4	**10**	**8**	10	2	3	6	4	1	1	1
	STS	1.63	**3**	**2.27**	0.7	0.74	1	1.6	1.5	0.65	0.83	1.55
$r/a = 0.55$	Occurrences	**10**	**10**	1	7	1	0	5	4	1	3	**8**
	STS	**2.8**	**2.6**	0.33	0.4	0.34	–	1.34	1.14	0.37	0.75	**1.72**
$r/a = 0.65$	Occurrences	4	3	1	5	6	**8**	2	**9**	1	5	6
	STS	1.11	0.66	0.49	0.96	1.18	**1.77**	0.52	**1.1**	0.97	1.28	1.5
$r/a = 0.75$	Occurrences	**10**	**7**	**10**	1	2	4	**10**	2	1	1	2
	STS	**3.34**	**1.2**	**1.34**	0.2	0.35	0.75	**1.85**	0.25	0.23	0.17	0.16
$r/a = 0.85$	Occurrences	**10**	**10**	2	**10**	2	4	3	3	2	4	0
	STS	**2.37**	**2**	0.64	**2.14**	0.61	0.73	0.57	0.66	0.45	0.7	–

consistent with typical carbon profiles of Fig. 1 with respect to the direction of the convective mechanism associated with u'. On the other hand, the coefficient related to R/L_n is rather constant throughout the radial domain. Also, note that the standard deviation of the coefficient b in the 10 best fits is relatively small, which underlines the consistency of such regressions with u' and R/L_n parameters.

III. GYROKINETIC AND NEOCLASSICAL MODELING METHODOLOGY

In this section, the modeling assumptions for the neoclassical and turbulent impurity transport are detailed. The total impurity flux is decomposed into a neoclassical and a turbulent component,

$$\Gamma_{tot} = \Gamma_{neo} + \Gamma_{turb}. \tag{2}$$

The neoclassical transport is computed using the code NEO and the turbulent transport using the gyrokinetic code GKW. The latter is first addressed, and the contributions of the neoclassical transport on the total carbon peaking factor are then considered. Mechanisms such as the impact of the neoclassical background on turbulent impurity transport[26] have been tested and found to be negligible for carbon transport in this database. Possible additional synergies between neoclassical and turbulent impurity transport are not considered in this study.

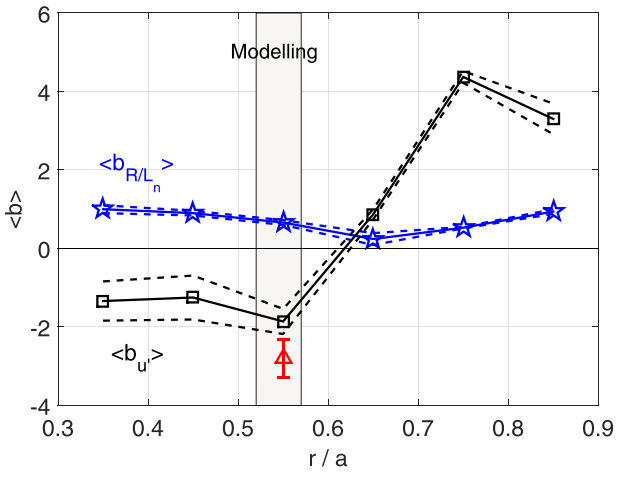

FIG. 3. Mean coefficient $\langle b \rangle$ for u' and R/L_n described in the text versus r/a. The standard deviation of $\langle b \rangle$ is also shown with dotted lines. The radial domain where simulations are performed is highlighted. The mean coefficient for u' found in the regression with the increased weight is also shown (red triangle).

A. Gyrokinetic modeling methodology

In all the following linear simulations, the local assumption is employed and justified ($\rho_* \sim 1/500$ at mid-radius). Parallel perturbations of the potential $\delta A_\parallel$ are retained but not the perpendicular component $\delta A_\perp$. The latter has been found to have negligible effects on impurity transport modeling for this database, although the normalised electron pressure $\beta_e = 2\mu_0 n_e T_e / B^2$ can reach values up to 1%. Collisions are modelled via the pitch-angle scattering operator together with an ad-hoc momentum restoring term (the effect of energy scattering is marginal for these ITG cases[27]). It includes collisions between deuterium, electrons, and carbon, hence retaining linear and non-linear effects of collisions such as the zonal flow damping through ion-ion collisions. For this database, the linear effect of ion-carbon collisions is found to be negligible at high collisionalities. Due to the presence of strong NBI in this database and hence strong toroidal rotation and its associated gradient, centrifugal effects and the Coriolis drifts are taken into account. Finally, the experimental magnetic field geometry, computed from EFIT, is used through the interface between GKW and the toroidal MHD equilibrium solver CHEASE.[28] Thus, the up-down asymmetry (symmetry breaking mechanism) is included in the modeling. In specific cases where sensitivity tests are performed on the magnetic shear and safety factor, the Miller parametrisation of the flux surfaces is also employed.[29]

After convergence tests, the following numerical grids are selected: $n_\mu = 12$, $n_{v_\parallel} = 64$, $n_s/n_{pt} = 32$, and $n_{pt} = 13$ for the number of points in the magnetic moment, parallel velocity, parallel direction, and the number of poloidal turns, respectively. In Fig. 4, growth rate spectra are shown for cases with low and medium experimental carbon concentrations. The trace and non-trace simulations are compared. It is

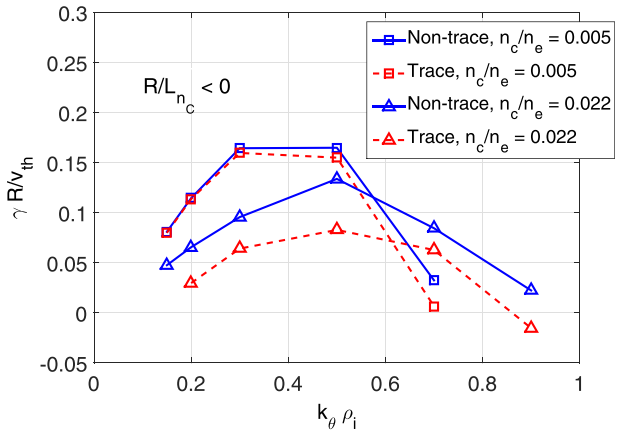

FIG. 4. Normalised growth rate versus the normalised poloidal wave number for low (squares) and medium (triangles) carbon density cases at $r/a = 0.55$. The trace assumption (dotted lines) is compared to the non-trace decomposition (full lines) used in this work.

shown that at low concentration ($n_c/n_e = 0.005$), the two assumptions converge. On the other hand for a medium (for this database) carbon concentration ($n_c/n_e = 0.022$), the ion temperature gradient instability is destabilised by the presence of impurities. This is due to the negative carbon peaking factor at this radial location and has been described in Refs. 40 and 41. In the following, carbon is not considered as a trace in the simulations (concentrations up to 4%), and the experimental density and gradients values are retained. The logarithmic ion density gradient is then computed from the quasi-neutrality equation assuming that carbon is the only impurity and neglecting the fast-ion contribution. When the fast-ion population, computed from the PENCIL code,[42] is taken into account, this yields to a reduction in the bulk ion logarithmic density gradient by typically ∼20%. No sign reversal of the logarithmic ion density gradient is observed.

To address the large number of entries in the database and build a statistically relevant comparison between the experiment and modeling, a quasi-linear approach is adopted.[30–33] This approach is based on the assumption that the characteristic turbulent diffusivity scales as

$$D = \frac{\gamma}{\langle k_\perp^2 \rangle} \tag{3}$$

with γ the most unstable linear growth rate and $k_\perp$ the perpendicular wave vector. This makes use of a characteristic time scale $\Delta t = 1/\gamma$ and a characteristic length scale $(\Delta x)^2 = 1/\langle k_\perp^2 \rangle$ given by

$$\langle k_\perp^2 \rangle = \frac{\int |\phi|^2 k_\perp^2 \mathrm{d}s}{\int |\phi|^2 \mathrm{d}s}, \tag{4}$$

which takes into account the extended structure of the electrostatic potential ϕ along the field line. In normalised units, the impurity flux can then be written as

$$\Gamma_{QL} = \sum_{k_\theta} \Gamma_{k_\theta} \frac{\gamma_{k_\theta}}{\langle k_\perp^2 \rangle}, \tag{5}$$

where Γ_{k_θ} is the flux surface averaged linear impurity flux for a given k_θ and normalised with the corresponding value of $\langle |\phi|^2 \rangle$. By default, the quasi-linear flux is assessed at $k_r \rho_i = 0$, but one could build more complex quasi-linear models including finite k_r contributions, see, e.g., Ref. 38. This flux can be further decomposed into a diffusive and a convective part,

$$\Gamma_{QL} = \frac{n}{R} D_{QL} \left(\frac{R}{L_n} + C_{T,QL} \frac{R}{L_T} + C_{u,QL} u' + C_{p,QL} \right) \tag{6}$$

with D_{QL}, $C_{T,QL}$, $C_{u,QL}$, and $C_{p,QL}$ the quasilinear diffusivity, thermo-diffusion coefficient, rotodiffusion coefficient, and constant pinch, respectively. These are directly linked to the diffusive and convective coefficients of each spectral component Γ_{k_θ} of the total quasi-linear flux Γ_{QL},

$$D_{QL} = \sum_{k_\theta} D_{k_\theta} \frac{\gamma_{k_\theta}}{\langle k_\perp^2 \rangle}, \tag{7}$$

$$C_{p,QL} = \sum_{k_\theta} D_{k_\theta} C_{p,k_\theta} \frac{\gamma_{k_\theta}}{\langle k_\perp^2 \rangle} / D_{QL}, \tag{8}$$

$$C_{T,QL} = \sum_{k_\theta} D_{k_\theta} C_{T,k_\theta} \frac{\gamma_{k_\theta}}{\langle k_\perp^2 \rangle} / D_{QL}, \tag{9}$$

$$C_{u,QL} = \sum_{k_\theta} D_{k_\theta} C_{u,k_\theta} \frac{\gamma_{k_\theta}}{\langle k_\perp^2 \rangle} / D_{QL}. \tag{10}$$

In the steady state and without carbon sources, the carbon peaking factor then directly follows:

$$\frac{R}{L_{nC}} = -C_{p,QL} - C_{T,QL} \frac{R}{L_T} - C_{u,QL} u'. \tag{11}$$

To separately evaluate the transport coefficients, four impurities are used in the simulations with different normalised gradients (similar to Ref. 39). The combination of these impurities is strictly equivalent to having one impurity species with experimental levels of concentration and gradients.

In all the subsequent quasi-linear estimates, the spectral range $k_\theta \rho_i = [0.15; 0.2; 0.3; 0.5; 0.7; 0.9]$ and $k_r \rho_i = 0$ have been used. As the carbon peaking factor only depends on the flux ratio, it is not sensitive to the saturation amplitude and is only a function of the spectral shape in $k_\theta \rho_i$. This makes the quasi-linear approach particularly suited to address the prediction of impurity peaking (the major difficulty of quasi-linear models is to predict the non-linear saturation level).

The size of the spectral range has also been extended to electron scales $k_\theta \rho_i = 50$, keeping the same mixing length rule for testing purposes. This yields not only a large electron heat flux generated by the Electron Temperature Gradient (ETG) driven mode but also a non-zero impurity flux. The poloidal wave number dependencies of the transport coefficients $C_{p,QL}$, $C_{u,QL}$, and $C_{T,QL}$ are illustrated in Fig. 5 for the same case as in Fig. 4, with $n_C/n_e = 0.022$. In the ITG range at low $k_\theta \rho_i$, outward contributions for thermo-diffusion $C_{T,QL}$ and rotodiffusion $C_{u,QL}$ and an inward contribution for the curvature pinch $C_{p,QL}$ are observed as predicted by

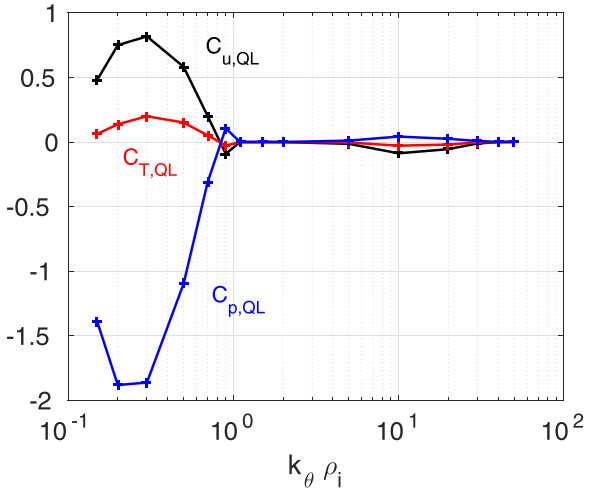

FIG. 5. Poloidal wave number dependencies of $C_{p,QL}$, $C_{u,QL}$, and $C_{T,QL}$ up to the ETG scales for the case of Fig. 4 with $n_C/n_e = 0.022$.

theory.[1] Going to the electron scales yields a sign change for these transport coefficients, concomitant with a sign change of the mode frequency. Including these scales leads to a significant increase in R/L_{n_C}. Nevertheless, the experimental ratio Q_i/Q_e is greatly underestimated due to the large Q_e generated by the ETG, which suggests that the impact of small scale turbulence, included using the mixing length estimate of Eq. (3), on R/L_{n_C} should be evaluated with a proper weighting. When an ad-hoc weighting of the electron scales is used to match the experimental value of Q_i/Q_e, the prediction of R/L_{n_C} becomes similar to the prediction with the ion scale contributions only.

A non-linear simulation has also been performed to verify the quasi-linear approach and quantitatively investigate non-linear mechanisms responsible for light impurity transport. The following gridsizes have been used: $n_\mu = 16$, $n_{v_\parallel} = 50$, $n_s/n_{pt} = 32$, 339 radial wave vectors, 15 binormal wave vectors with $k_\theta \rho_i$ ranging from 0 to 1.1, and $k_r \rho_i$ ranging from –21 to + 21. To evaluate the impact of background $E \times B$ shearing, two non-linear simulations have been performed with and without this mechanism.

Time traces of the non-linear simulation with $E \times B$ shearing are shown in Fig. 6, and a comparison with the quasi-linear spectrum of the carbon flux is performed in Fig. 7. Electromagnetic contributions to the electron and ion heat fluxes are found to be negligible compared to the electrostatic part, although $\beta_e = 1\%$. The effect of $E \times B$ shearing is significant ($u' = 1.55$) and reduces the saturation amplitude of the non-linear heat fluxes as expected.

The quasi-linear carbon flux spectrum, after rescaling its amplitude (which has no effect on the carbon peaking factor modeling as stated above), is found to peak roughly at the same poloidal wave number than the corresponding non-linear spectrum (also rescaled) without $E \times B$ shearing (summed over the $k_r \rho_i$). Contributions at higher poloidal wave numbers are overestimated in the quasi-linear estimate (for this case). It can also be shown that the non-linear carbon flux summed over the poloidal wave numbers peaks at $k_r \rho_i = 0$, which justifies the choice made for the quasi-linear approach. Nevertheless, this assumption will also be tested

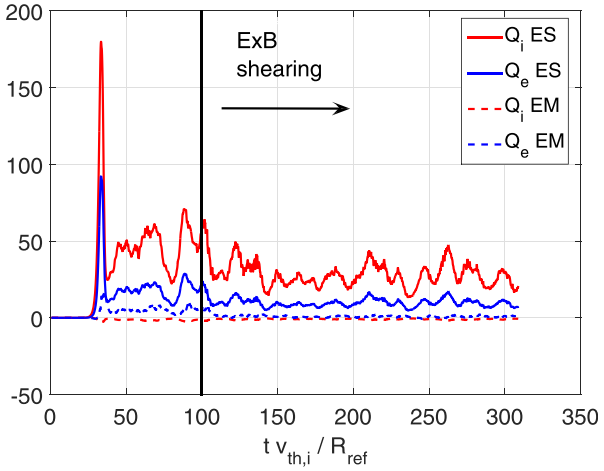

FIG. 6. Time traces of the normalised non-linear electron and ion heat fluxes. Electrostatic/electromagnetic contributions to the fluxes are shown as solid/dashed lines. $E \times B$ shearing is added to the simulation at the normalised time $tv_{th,i}/R_{ref} = 100$.

in Sec. IV where the quasi-linear peaking factor is evaluated for nonzero $k_r \rho_i$.

B. Neoclassical contributions

To account for the neoclassical contributions in the modeling of R/L_{n_C}, the same methodology as in Ref. 2 is used. The quasi-linear turbulent fluxes are rescaled so that they match the experimental heat fluxes Q^{exp},

$$\Gamma_C = \Gamma_{C,neo} + \Gamma_{C,turb}^{QL} \frac{Q_i^{\exp} - Q_i^{neo}}{Q_i^{QL}}. \tag{12}$$

For a zero total carbon flux (stationary phase and no carbon sources in the core), this equation yields the following expression of the peaking factor:

$$\frac{R}{L_{n_C}} = -\frac{RV^{QL}/\chi_i^{QL} + RV^{neo}/\chi_i^{an}}{D^{QL}/\chi_i^{QL} + D^{neo}/\chi_i^{an}}, \tag{13}$$

where

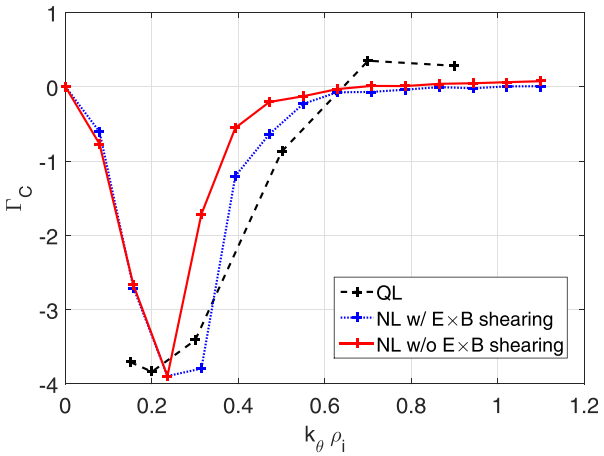

FIG. 7. Quasi-linear and non-linear spectra of the normalised carbon flux in $k_\theta \rho_i$. The spectra have been rescaled in order to compare the shape and not the saturation.

$$V^{QL} = D^{QL}\left(C_{T,QL}\frac{R}{L_T} + C_{u,QL}u' + C_{p,QL}\right). \quad (14)$$

The super/subscripts *neo* and *QL* stand for neoclassical and turbulent quantities. χ_i^{an} and χ_i^{QL} are the anomalous and quasi-linear heat diffusivities, respectively, computed from $Q_i^{\exp} - Q_i^{neo}$ for the former and Q_i^{QL} for the latter, using the relation $Q_i = (n_i T_i/R)\chi_i R/L_{T_i}$.

In Fig. 8, the carbon peaking factor computed from Eq. (13) is compared to the turbulent R/L_{n_C} computed from Eq. (11). It is shown that for positive predicted values of R/L_{n_C}, neoclassical contributions are negligible. On the other hand for values of R/L_{n_C} close to zero or for negative values, neoclassical contributions are not negligible and should be taken into account to attempt quantitative comparisons with the experiment. From now on, the modelled peaking factor always takes into account the neoclassical contributions.

Finally, it is to be noted that the first order carbon toroidal velocity computed from NEO (including diamagnetic contributions) at the low field side is below 5% of the measured carbon toroidal velocity for this database. Thus, the toroidal velocity measured is, to a good approximation, the $E \times B$ toroidal velocity.

IV. EXPERIMENT VS SIMULATIONS

In this section, the simulations focus at $r/a = 0.55$, where the carbon profiles are experimentally very hollow. For two particular cases, the comparison is extended to the radial domain $r/a = 0.45$–0.85.

A. Experimental and modelled R/L_{n_C} at r/a=0.55

To underline the importance of rotodiffusion on light impurity transport, the modelled carbon peaking factor is plotted versus the normalised toroidal rotation gradient u' and compared to corresponding experimental values in Fig. 9. It is to be noted that in these simulations, ITG turbulence is dominant.

Including the rotodiffusion term in the modeling of R/L_{n_C} yields flatter and even hollow profiles for sufficiently large values of u'. This result goes in the same direction as found in AUG,[2,3] i.e., outward rotodiffusion plays a quantitatively important role in establishing the light impurity peaking factor going from positive to negative values. Although this effect is quite strong in reversing the sign of the peaking factor, most experimental values lie below the modelled R/L_{n_C} by a significant amount.

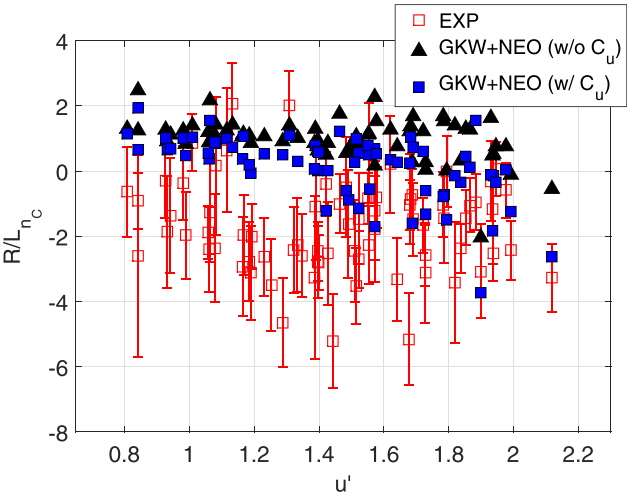

FIG. 9. Carbon peaking factor at $r/a = 0.55$ versus the normalised toroidal rotation gradient u'. The modeling results are shown with/without rotodiffusion and compared to the experimental values.

As we have seen in the multilinear regressions of Sec. II, R/L_{n_C} is strongly connected to R/L_n. In Fig. 10, comparisons between modelled and experimental R/L_{n_C} versus R/L_n are shown. The discrepancy between the theory and experiment is observed over the whole R/L_n domain. Therefore, there is no clear correlation between the theoretical and experimental mismatch and R/L_n, or in other words, the experimental correlation observed between R/L_{n_C} and R/L_n is partly recovered in the modeling.

After extensive analysis of the disagreement between theoretical and experimental R/L_{n_C} in the parameter space, the modelled and experimental peaking factors versus the normalised collisionality ν_* are shown in Fig. 11, which is correlated with R/L_n and T_e/T_i. The ν_* dependency unravels two different regimes. At low ν_*, the agreement between

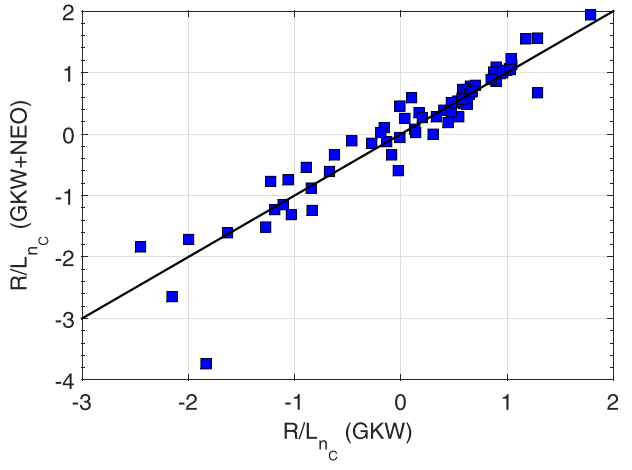

FIG. 8. Turbulent and neoclassical carbon peaking factors computed from GKW and NEO compared to turbulent R/L_{n_C} only.

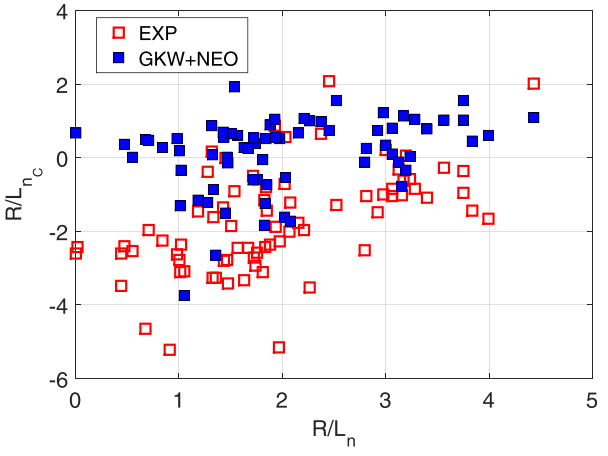

FIG. 10. Carbon peaking factor versus R/L_n at $r/a = 0.55$. Experimental error bars have been omitted for clarity.

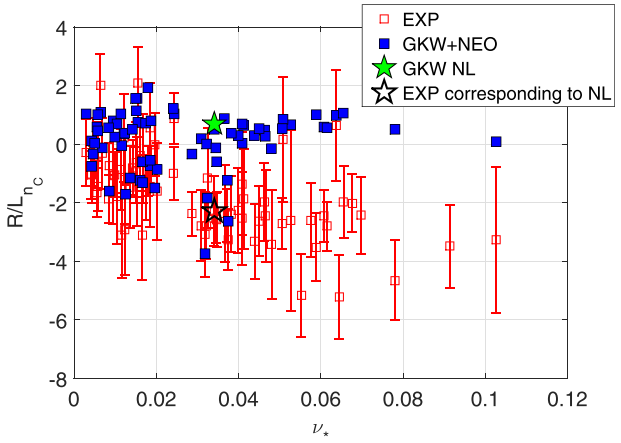

FIG. 11. Carbon peaking factor at $r/a = 0.55$ versus the normalised collisionality ν_*. The modeling results using the quasi-linear approach are compared to the experimental values. The result of a non-linear simulation is also shown, where the disagreement between the experimental and modelled value is substantial.

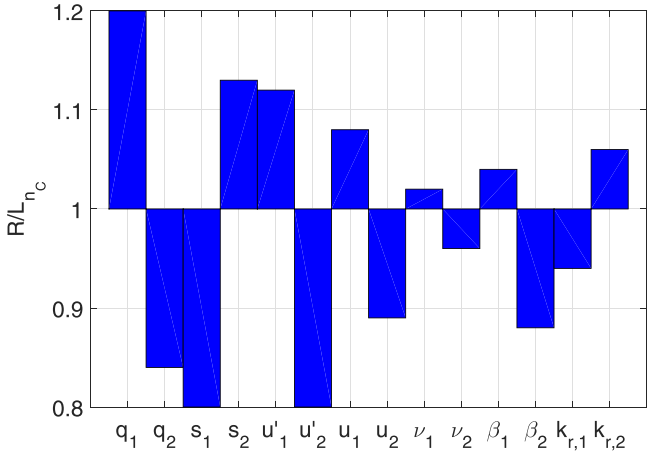

FIG. 12. Carbon peaking factor obtained for different values of the corresponding plasma parameters represented on the x-axis for the case at $\nu_* = 0.06$. The values of these parameters are gathered in Table IV and are varied around their nominal values.

modeling and the experiment is satisfactory, within the experimental error bars. On the other hand, at higher ν_*, the disagreement is systematic, and while the predictions are peaked (positive R/L_{n_C}), the experimental profiles are significantly hollow (negative R/L_{n_C}). A non-linear simulation, presented in Sec. III and performed where the disagreement between the theory and experiment is substantial ($R/L_{n_C}^{\text{exp}} = -2.1$, $R/L_{n_C}^{QL} = 0.6$), for the parameters of Table III, confirms the validity of the quasi-linear approach: the non-linear peaking factor $R/L_{n_C} = 0.7$ is almost identical to the quasi-linear estimate. $E \times B$ shearing not only impacts the rotodiffusion coefficient due to symmetry breaking but also modifies the curvature pinch and thermo-diffusion, yielding a marginal change in R/L_{n_C} (0.72) for this case. This suggests that the quasi-linear approach is satisfactory in this domain of parameters and that the discrepancy observed with the experiment does not come from non-linear mechanisms such as $E \times B$ shearing or sub-dominant modes. However, this does not rule out possible missing ingredients related to non-linear physics. Finally, the same conclusions can be drawn when comparing the experimental and predicted values of R/L_{n_C} versus T_e/T_i due the strong correlation with ν_* (see Table V). At $T_e/T_i < 1$, the theory and experiment are in good agreement, whereas for $T_e/T_i > 1$, a systematic disagreement occurs.

Several sensitivity tests have been performed for a case at $\nu_* = 0.06$ to assess the role of important parameters such as the magnetic shear and safety factor in the discrepancy observed. The predicted R/L_{n_C} for this case is 1, whereas the experimental value is $R/L_{n_C}^{\text{exp}} = -3.5$. These tests are shown in Fig. 12 together with the corresponding values of the plasma parameters in Table IV. The latter have been varied independently around their nominal values. The sensitivity of R/L_{n_C} with R/L_n, R/L_{T_i}, T_e/T_i, and R/L_{T_e} not shown in Fig. 12 has also been checked, yielding modifications of the carbon peaking factor below 5% for a 20% variation of these parameters. All parameters have been consistently changed in NEO and GKW. The most sensitive parameters with respect to variations of the carbon peaking factor are the safety factor as also shown in[3] and u'. Increasing these parameters flattens the predicted carbon profile as expected. Nonetheless, the values needed to recover the experimental R/L_{n_C} are far beyond the error bars. We note that, although toroidal rotation is large, the carbon peaking predictions are not particularly sensitive to finite $k_r\rho_i$. Sensitivity tests have also been performed for the case in Table III, yielding the same results, that is, discrepancies between predicted and experimental values of R/L_{n_C} are robust with respect to variations of plasma parameters.

At this point, it is clear that an ingredient is missing in the modeling of the carbon peaking factor, and this ingredient appears to be linked to the normalised collisionality ν_* (or T_e/T_i). The strong linear relation of the experimental peaking factor with u' found in Sec. II underlines a possible stronger outward convection mechanism than what is obtained in simulations. This improved convection should scale with ν_* (or T_e/T_i).

TABLE III. Input parameters for the non-linear simulation corresponding to shot number 68660 at t = 9.2 s.

$\hat{s}$	q	ϵ	T_e/T_i	R/L_{n_e}	R/L_{T_e}	R/L_{T_i}	u'	β	u	ν_*
1.01	1.57	0.17	1.186	1.98	4.62	6.78	1.55	1%	0.22	0.034

B. Multi-channel analysis

To shed some light on the regime where experimental and theoretical R/L_{n_C} are in disagreement, the heat and momentum channels are scrutinised (Fig. 13). The problem of the turbulent saturation amplitude is set aside by looking at the ratio of the ion momentum flux to the ion heat flux (Π_i/Q_i) and the electron to ion heat flux ratio (Q_e/Q_i). The total ion momentum flux is considered here, that is, summed over the deuterium and carbon species. The carbon heat flux is less than 3% of the ion heat flux and is not included. Their experimental counterparts are computed from the steady state momentum and heat transport equations, considering the particle, torque, and heat NBI/ICRH sources together with electron-ion equipartition and Ohmic heating. The experimental ion momentum flux is corrected from the

TABLE IV. Values used for the sensitivity tests of Fig. 12. The nominal values are also listed.

Parameter	β_1	β_2	q_1	q_2	$\hat{s}_1$	$\hat{s}_2$	u'_1	u'_2	u_1	u_2	$\nu_{*,1}$	$\nu_{*,2}$	$k_{r,1}\rho_i$	$k_{r,2}\rho_i$
Values of Fig. 12	0.1%	0.5%	1.5	3.5	0.4	1.5	0.9	2.2	0.1	0.3	0.04	0.09	−0.1	0.1
Nominal values	0.26%		2.6		0.85		1.5		0.2		0.06		0	

momentum carried by the particle flux.[15] The radiated power at the mid-radius is found to be negligible.

Considering only the NBI heated plasmas, the predicted and experimental Π_i/Q_i feature two opposite trends with ν_* (or T_e/T_i): predicted values increase with ν_*, while experimental values decrease. These trends are less clear for plasmas with non-zero ICRH, especially for $0.04 < \nu_* < 0.07$. The non-linear Π_i/Q_i is ∼20% lower than the quasi-linear estimate (but still ∼3 times higher than the experimental value), and $E \times B$ shearing does not affect significantly Π_i/Q_i in this regime.

It is known that both the momentum flux and impurity rotodiffusion stem from parallel symmetry breaking mechanisms.[1,18] This peculiarity could underline a common missing ingredient in the modeling, linked to parallel symmetry, thus leading to inaccurate predictions at high ν_* of the ion momentum flux and the carbon peaking factor altogether.

In contrast, the predicted ratio Q_i/Q_e in Fig. 13(b) is shown to be systematically higher than the experimental ratio, which is consistent with low $k_\theta\rho_i$ computations (ETG scales are excluded and would contribute to Q_e). While no particular care has been given matching the experimental heat flux ratio (nontrivial additional physics could be needed such as multi-scale interactions[34,35] or non-linear fast ion stabilisation[36]), no link between the theoretical discrepancies and ν_* is observed for this channel.

C. Carbon profiles at low and high collisionalities

To gain more insight into the two collisionality regimes underlined in Sec. IV A, simulations are performed over a larger fraction of the radial domain for two particular cases, one at low ν_* (0.012) and one at higher ν_* (0.034) from Table III.

In Fig. 14, the predicted profiles of R/L_{n_C} are compared to the experimental one. Again modelled values with and without rotodiffusion are shown. For the low collisionality case [Fig. 14(b)], the correspondence between prediction and the experiment is strikingly accurate, provided that rotodiffusion is taken into account, the latter being a critical ingredient for $r/a < 0.6$.

On the contrary, for the high collisionality case [Fig. 14(a)], agreement between the experiment and theory is very poor, except at one radial position where both profiles cross each other, with the experimental profile showing a strong radial variation from $R/L_{n_C} \sim -4$ to $R/L_{n_C} \sim 6$ at the edge. Rotodiffusion does not significantly affect the predictions in this case but tends to flatten/peak the carbon profile in the core/edge. The change in the sign of rotodiffusion at the edge (in both collisionality cases) is due to a change in the turbulent drive going from a temperature gradient driven mode to a density gradient driven mode. Discrepancies at inner (hollow profile) and outer (peaked profile) radii could not only stem from very different physical mechanisms but also have a similar effect (enhancement) on rotodiffusion as we have seen a strong correlation of the carbon peaking factor with u' over the whole radial domain in Sec. II.

These results not only demonstrate the relevance of the standard modeling approach adopted but also show that there are limitations where it is incomplete and requires additional, yet unknown, physical ingredients linked to the collisionality (or T_e/T_i). This should motivate further studies on high collisionality cases to identify the physics behind such experimental variations of R/L_{n_C}.

V. CONCLUSIONS

A database of H-modes in JET-C, extensively used to study momentum and particle transport properties in the

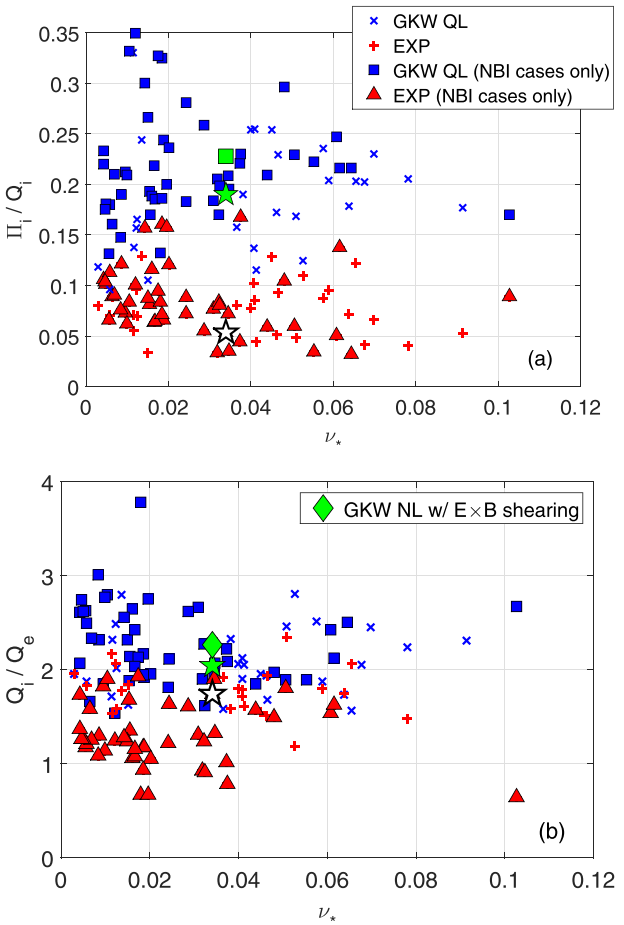

FIG. 13. Normalised ratio of the ion momentum flux with the ion heat flux (a) and the ion to electron heat flux ratio (b). Quasi-linear and non-linear (green pentagrams) values are compared with the experiment. The open pentagram and green square correspond to the experimental and predicted (quasi-linear) values, respectively, associated with the non-linear simulation. The effect of $E \times B$ shearing is shown only for Q_i/Q_e where modifications of this ratio are visible (it also matches the associated quasi-linear value).

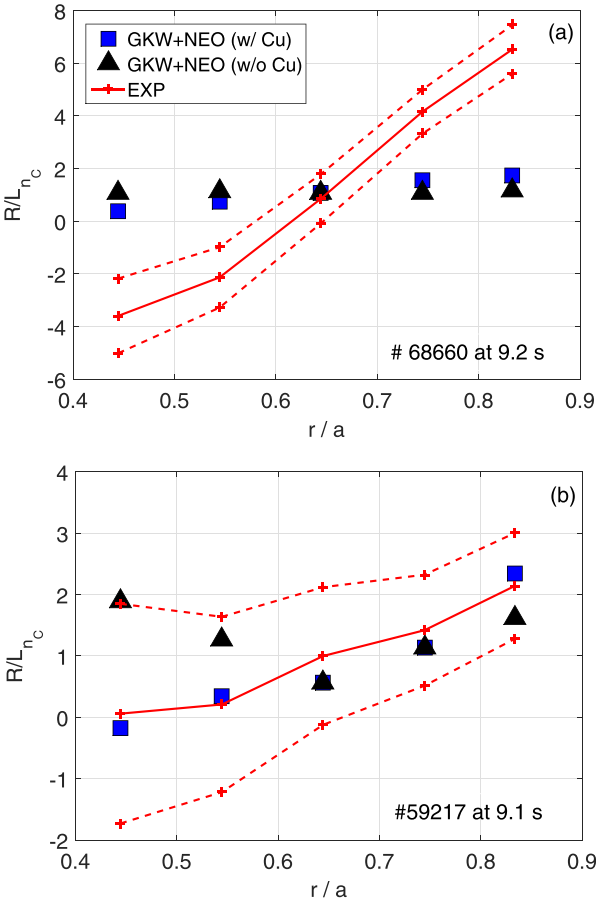

FIG. 14. Comparison of the carbon peaking factor profiles between fits from experimental carbon profiles (with corresponding error bars in dashed lines) and modelled values with/without rotodiffusion. Two particular cases are shown: at high (a) and low (b) ν_*, 0.034 and 0.012, respectively.

past, is scrutinised in this work for carbon transport. These discharges feature very hollow carbon density profiles with peaking factors (R/L_{n_C}) up to –5 at the mid-radius and peaked at the plasma edge. From multi-linear regressions, the relevant parameters to describe these profile shapes are the normalised toroidal angular rotation frequency gradient u' and the normalised density gradient R/L_n. The former suggests an important role of the convection associated with this gradient, while the dependency on R/L_n underlines additional physics mechanisms such as the collisionality (R/L_n and the collisionality are strongly correlated in this database). These types of profiles are very favorable in terms of impurity accumulation avoidance, which motivated a thorough study and understanding of the carbon transport in these plasmas.

To do so, gyrokinetic and neoclassical simulations are performed for a large number of database entries (∼100) at the mid-radius. To tackle the large number of simulations required, a quasi-linear approach is adopted and supported by non-linear simulations. Neoclassical transport of carbon is shown to be non-negligible compared to the quasi-linear turbulent transport, in particular where R/L_{n_C} is predicted to be negative (from turbulent transport) and thus connected to high values of u'. Therefore, comparisons between theoretical and experimental values of R/L_{n_C} are performed using the turbulent and neoclassical contributions. Two important results arise from this comparison and are divided into two regimes, at low and high normalised collisionality ν_* or at $T_e/T_i < 1$ and $T_e/T_i > 1$, respectively (these two parameters being strongly correlated in this database).

At low ν_*, the agreement between the theory and the experiment is satisfactory, provided that rotodiffusion is taken into account. The latter provides an additional outward convection (together with thermo-diffusion) that is substantial in these NBI heated plasmas and confirms the previous results on the importance of this mechanism.[2,3]

In contrast, at high ν_*, the agreement is systematically poor. This is also confirmed by non-linear simulations and extensive sensitivity tests of the modelled result with variations of the input plasma parameters. The effect of non-linear $E \times B$ shearing is found to be negligible and does not fill the gap between predicted and experimental R/L_{n_C}.

A multi-channel analysis has been performed, i.e., comparisons of the experimental and modelled ratios of ion momentum flux to ion heat flux (Π_i/Q_i) and ion to electron heat fluxes (Q_i/Q_e). Predicted and experimental values of Π_i/Q_i feature two opposite trends with ν_*. On the other hand, discrepancies between experimental and theoretical Q_i/Q_e are found to be independent of the normalised collisionality ν_*. The similar disagreement for the ion momentum flux and R/L_{n_C} could hint toward a common missing ingredient linked to parallel symmetry breaking mechanisms and ν_*.

Finally, comparisons of the theoretical and experimental R/L_{n_C} are performed over a large fraction of the minor radius $r/a = 0.45$–0.85 for low and high collisionality cases. At low ν_*, the agreement is very good over the whole radial domain, while at high ν_*, the experimental R/L_{n_C} features strong radial variations which are not captured by the modeling. At the mid-radius, the experimental carbon peaking factor is over-estimated, while at $r/a \sim 0.8$, it is under-estimated. The strong experimental hollowness (also observed at ASDEX Upgrade[37]) in the core and peaking at the edge could stem from different physical mechanisms. Further studies are needed to identify the mechanisms currently missing in the light impurity transport modeling paradigm.

ACKNOWLEDGMENTS

The authors acknowledge very fruitful discussions with A. Kappatou, R. McDermott, N. Bonanomi, and P. Mantica. Part of this work was performed using HPC resources from GENCI-IDRIS (Grant No. 2014-056892). Part of this work was granted access to the HPC resources of Aix-Marseille Université financed by the project Equip@Meso (ANR-10-EQPX-29-01) of the program "Investissements d'Avenir" supervised by the Agence Nationale pour la Recherche. This work was carried out within the framework EUROfusion Consortium and received funding from the Euratom research and training programme 2014–2018 under grant agreement No. 633053. The views and opinions expressed herein do not necessarily reflect those of the European Commission.

APPENDIX: CORRELATION TABLE AT r/a=0.55

To determine correlations in the database studied in this paper, the following definition of the correlation coefficient $r_c(y, z)$ between the variables y and z has been used:

TABLE V. Correlation table at $r/a = 0.55$ using Eq. (A1). Values above 0.2 are highlighted in bold.

	u'	R/L_n	R/L_{T_i}	R/L_{T_e}	β	ρ_*	$\hat{s}$	q	ν_*	T_e/T_i	M_D	R/L_{n_C}
u'	1	0.08	**0.36**	0	0.07	0.14	0	0	0	0	0.14	0.06
R/L_n	0.08	1	0	0	0	0	0	0	**0.5**	0.19	0	0.13
R/L_{T_i}	**0.36**	0	1	0	0	0.13	0	0	0	0	0	0
R/L_{T_e}	0	0	0	1	0.1	0.15	0	0.06	0.07	0.1	0.17	0
β	0.07	0	0	0.1	1	**0.6**	0	**0.44**	0.12	0.2	**0.31**	0
ρ_*	0.14	0	0.13	0.15	**0.6**	1	0	**0.27**	**0.42**	**0.29**	0.23	0
$\hat{s}$	0	0	0	0	0	0	1	0	0	0	0	0
q	0	0	0	0.06	**0.44**	**0.27**	0	1	0.16	0.17	0.13	0.09
ν_*	0	**0.5**	0	0.07	0.12	**0.42**	0	0.16	1	**0.72**	0.2	0.16
T_e/T_i	0	0.19	0	0.1	0.2	**0.29**	0	0.17	**0.72**	1	**0.4**	0.17
M_D	0.14	0	0	0.17	**0.31**	0.23	0	0.13	0.2	**0.4**	1	0
R/L_{n_C}	0.06	0.13	0	0	0	0	0	0.09	0.16	0.17	0	1

$$r_c(y,z) = 1 - \frac{\sum_{i=1}^{N} (y_i - y_{fit,i})^2}{NV(y)} \tag{A1}$$

with N the number of points in the database, y_i the ith value of the considered variable y, $y_{fit}(z)$ the linear fit of y with respect to z ($y_{fit} = a \times z + b$), and $y_{fit,i} = a \times z_i + b$. $V(y)$ is the variance defined by

$$V(y) = \frac{1}{N} \sum_{i=1}^{N} (y_i - m)^2 \tag{A2}$$

with m the mean value of y_i.

This definition of the correlation parameter yields a perfect correlation ($r_c = 1$) for $y_i = y_{fit,i}$ for each $i = 1$ to N and no correlation ($r_c = 0$) for $y_{fit} = m$. The latter condition is fulfilled when the slope of the linear function $y_{fit}(z)$ is zero. Table V gather these correlations for a set of physically relevant parameters (defined in Sec. II B): u', R/L_n, R/L_{T_i}, R/L_{T_e}, β, $\rho_* = \rho_i/a$, q, $\hat{s}$, $\nu_* = \nu_{ei} q/\epsilon^{3/2}$, T_e/T_i, M_D, and R/L_{n_C}. Correlations below $r_c = 0.05$ are set to zero and are not discussed.

[1]C. Angioni, Y. Camenen, F. J. Casson, E. Fable, R. M. McDermott, A. G. Peeters, and J. E. Rice, Nucl. Fusion **52**, 114003 (2012).
[2]C. Angioni, R. M. McDermott, E. Fable, R. Fischer, T. Pütterich, F. Ryter, G. Tardini, and the ASDEX Upgrade Team, Nucl. Fusion **51**, 023006 (2011).
[3]F. J. Casson, R. M. McDermott, C. Angioni, Y. Camenen, R. Dux, E. Fable, R. Fischer, B. Geiger, P. Manas, L. Menchero, G. Tardini, and the ASDEX Upgrade Team. Nucl. Fusion **53**, 063026 (2013).
[4]H. Nordman, A. Skyman, P. Strand, C. Giroud, F. Jenko, F. Merz, V. Naulin, and T. Tala, and the JET-EFDA Contributors, Plasmas. Phys. Controlled Fusion **53**, 105005 (2011).
[5]A. Skyman, L. Fazendeiro, D. Tegnered, H. Nordman, J. ANderson, and P. Strand, Nucl. Fusion **54**, 013009 (2013).
[6]D. R. Mikkelsen, M. Bitter, L. Delgado-Aparicio, K. W. Hill, M. Greenwald, N. T. Howard, J. W. Hughes, J. E. Rice, M. L. Reinke, Y. Podpaly, Y. Ma, J. Candy, and R. E. Waltz, Phys. Plasmas **22**, 062301 (2015).
[7]D. R. Mikkelsen, K. Tanaka, M. Nunami, T.-H. Watanabe, H. Sugama, M. Yoshinuma, K. Ida, Y. Suzuki, M. Goto, S. Morita, B. Wieland, I. Yamada, R. Yasuhara, T. Tokuzawa, T. Akiyama, and N. A. Pablant, Phys. Plasmas **21**, 082302 (2014).
[8]A. Kappatou, Ph.D. thesis, Eindhoven University of Technology, The Netherlands, 2014.
[9]A. Kappatou, R. M. McDermott, C. Angioni, T. Pütterich, R. Dux, R. J. E. Jaspers, E. Viezzer, M. Cavedon, R. Fischer, M. Willensdorfer, G. Tardini, the EUROfusion MST1 Team, and the ASDEX Upgrade Team, in *42nd EPS Conference on Plasma Physics* (2015).
[10]M. R. Wade, W. A. Houlberg, and L. R. Baylor, Phys. Rev. Lett. **84**, 282 (2000).
[11]N. T. Howard, M. Greenwald, D. R. Mikkelsen, M. L. Reinke, A. E. White, D. Ernst, Y. Podpaly, and J. Candy, Nucl. Fusion **52**, 063002 (2012).
[12]C. Angioni, P. Mantica, T. Pütterich, M. Valisa, M. Baruzzo, E. A. Belli, P. Belo, F. J. Casson, C. Challis, P. Drewelow *et al.*., Nucl. Fusion **54**, 083028 (2014).
[13]F. J. Casson, C. Angioni, E. A. Belli, R. Bilato, P. Mantica, T. Odstrcil, T. Pütterich, M. Valisa, L. Garzotti, C. Giroud, J. Hobirk, C. F. Maggi, J. Mlynar, and M. L. Reinke, Plasma Phys. Controlled Fusion **57**, 014031 (2015).
[14]M. Maslov, C. Angioni, H. Weisen, and JET-EFDA Contributors, Nucl. Fusion **49**, 075037 (2009).
[15]H. Weisen, Y. Camenen, A. Salmi, T. W. Versloot, P. C. de Vries, M. Maslov, T. Tala, M. Beurskens, C. Giroud, and JET-EFDA Contributors, Nucl. Fusion **52**, 042001 (2012).
[16]H. Weisen, Y. Camenen, A. Salmi, T. W. Versloot, P. C. de Vries, M. Maslov, T. Tala, M. Beurskens, C. Giroud, and JET-EFDA Contributors, Nucl. Fusion **52**, 114024 (2012).
[17]C. Angioni and A. G. Peeters, Phys. Rev. Lett. **96**, 095003 (2006).
[18]Y. Camenen, A. G. Peeters, C. Angioni, F. J. Casson, W. A. Hornsby, A. P. Snodin, and D. Strintzi, Phys. Plasmas **16**, 012503 (2009).
[19]E. A. Belli and J. Candy, Plasma Phys. Controlled Fusion **51**, 075018 (2009).
[20]A. G. Peeters, Y. Camenen, F. J. Casson, W. A. Hornsby, A. P. Snodin, D. Strintzi, and G. Szepezi, Comput. Phys. Commnun. **180**, 2650 (2009).
[21]L. L. Lao, H. S. John, R. D. Stambaugh, A. G. Kellman, and W. Pfeiffer, Nucl. Fusion **25**, 1611 (1985).
[22]C. Giroud, A. G. Meigs, C. R. Negus, K.-D. Zastrow, T. M. Biewer, and T. W. Versloot, Rev. Sci. Instrum. **79**, 10F525 (2008).
[23]A. Bortolon, Y. Camenen, A. N. Karpushov, B. P. Duval, Y. Andrebe, L. Dederspiel, and O. Sauter, and the TCV Team. Nucl. Fusion **53**, 023002 (2013).
[24]C. Angioni, H. Weisen, O. J. W. F. Kardaun, M. Maslov, A. Zabolotsky, C. Fuchs, L. Garzotti, C. Giroud, B. Kurzan, P. Mantica *et al.*., Nucl. Fusion **47**, 1326 (2007).
[25]C. Angioni, E. Fable, M. Greenwald, M. Maslov, A. G. Peeters, H. Takenaga, and H. Weisen, Plasma Phys. Controlled Fusion **51**, 124017 (2009).
[26]P. Manas, W. A. Hornsby, C. Angioni, Y. Camenen, and A. G. Peeters, Plasma Phys. Controlled Fusion **59**, 035002 (2017).
[27]P. Manas, Y. Camenen, S. Benkadda, W. A. Hornsby, and A. G. Peeters, Phys. Plasmas **22**, 062302 (2015).
[28]H. Lütjens, A. Bondeson, and O. Sauter, Comput. Phys. Commun. **97**, 219 (1996).
[29]R. L. Miller, M. S. Chu, J. M. Greene, Y. R. Lin-Liu, and R. E. Waltz, Phys. Plasmas **5**, 973 (1998).
[30]F. Jenko, T. Dannert, and C. Angioni, Plasma Phys. Controlled Fusion **47**, B195 (2005).
[31]M. Kotschenreuther, W. Dorland, M. A. Beer, and G. W. Hammett, Phys. Plasmas **2**, 2381 (1995).

[32]J. E. Kinsey, G. M. Staebler, and R. E. Waltz, Phys. Plasmas **15**, 055908 (2008).
[33]A. Casati, C. Bourdelle, X. Garbet, F. Imbeaux, J. Candy, F. Clairet, G. Dif-Pradalier, G. Falchetto, T. Gerbaud, V. Grandgirard *et al*.., Nucl. Fusion **49**, 085012 (2009).
[34]N. T. Howard, C. Holland, A. E. White, M. Greenwald, and J. Candy, Nucl. Fusion **56**, 014004 (2016).
[35]S. Maeyama, Y. Idomura, T.-H. Watanabe, M. Nakata, M. Yagi, N. Miyato, A. Ishizawa, and M. Nunami, Phys. Rev. Lett. **114**, 255002 (2015).
[36]J. Citrin, F. Jenko, P. Mantica, D. Told, C. Bourdelle, J. Garcia, J. W. Haverkort, G. M. D. Hogeweij, T. Johnson, and M. J. Pueschel, Phys. Rev. Lett. **111**, 155001 (2013).
[37]M. N. A. Beurskens, M. G. Dunne, L. Frassinetti, M. Bernert, M. Cavedon, R. Fischer, A. Järvinen, A. Kallenbach, F. M. Laggner, R. M. McDermott *et al*.., Nucl. Fusion **56**, 056014 (2016).
[38]G. M. Staebler, R. E. Waltz, J. Candy, and J. E. Kinsey, Phys. Rev. Lett. **110**, 055003 (2013).
[39]C. Angioni, R. Dux, E. Fable, A. G. Peeters, and the ASDEX Upgrade Team, Plasma Phys. Controlled Fusion **49**, 2027 (2007).
[40]J. Q. Dong and W. Horton, Phys. Plasmas **2**, 3412 (1995).
[41]C. Estrada-Mila, J. Candy, and R. E. Waltz, Phys. Plasmas **12**, 022305 (2005).
[42]C. D. Challis, J. G. Cordey, H. Hamnén, P. M. Stubberfield, J. P. Christiansen, E. Lazzaro, D. G. Muir, D. Stork, and E. Thompson, Nucl. Fusion **29**, 563 (1989).